Detailed experimental and numerical analysis of flow field for a vertical axis wind turbine with auxiliary blades

F. Arpino[1], G. Cortellessa[1], M. Scungio[2], G. Fresilli[1], A. Facci[2], A. Frattolillo[3]

[1]*Department of Civil and Mechanical Engineering, University of Cassino and Southern Lazio, Cassino (FR), Italy*
[2]*Department of Economics, Engineering, Society and Business Organization, University of Tuscia, Viterbo, Italy*
[3]*Department of Civil and Environmental Engineering and Architecture, University of Cagliari, Cagliari, Italy*

Abstract

VAWT are very interesting in-home applications and can be adopted in power generation at low wind speed. Significant research activity has been carried out to improve VAWTs performance and the ability to accurately reproduce flow field around turbine blades by CFD techniques. Numerical results are typically compared to experiments only in terms of bulk power and torque generated by the rotor. In this paper the authors propose an experimental and numerical investigation of detailed flow field around a pair of blades installed on an innovative Darrieus-type VAWT. In scale numerical analysis, carried out by some of the authors in a previous publication and validated by using bulk data collected during the wind tunnel experiments, evidenced the advantages in terms of torque and power of this configuration. The objective of the work consists in the detailed flow field experimental analysis, by employing the Particle Image Velocimetry (PIV) technique, of a scaled prototype of the turbine blades, realized by 3D printing. PIV measurements allowed proper validation of the numerical model for a selected wind speed. The validated numerical tool represents a powerful tool to analyze different geometric configurations and in order to improve performance at low wind speed and self-starting ability.

Keywords: *Vertical Axis Wind Turbine; Particle Image Velocimetry; CFD validation; Darrieus-style wind turbines, PIV uncertainty analysis*

1. INTRODUCTION

Wind turbines are mainly classified by means of their axis of rotation: Horizontal Axis Wind Turbines (HAWT) and Vertical Axis Wind Turbines (VAWT). VAWT, in respect to the HAWT, are able to receive wind from different directions and allow to fix the generator at the bottom of the rotor and not on the tower. On the other hand, the turbulence phenomena over the blades are complex because the attack angle is variable with respect to the wind path [1].

Typical VAWT are represented by: i) the drag-based Savonius type, used mainly for small-scale power applications because of their low energy conversion efficiency [2]; ii) Darrieus type working

on the basis of the lift forces acting on the blades, characterized by higher energy conversion efficiency but poor self-starting capability [3]. For this reason, it is more interesting to study the domestic Darrieus turbines then the large-scales ones, presenting high problems in start-up their rotation [4]. CFD (Computational Fluid Dynamics) procedures represent a support to the experiments on wind turbines allowing to investigate the performances of different geometrical configurations with reduced times and costs [5]. CFD analysis if not validated can be affected by errors due to different factor as: the model geometry, the domain discretization, the selected boundary conditions, the selected turbulence model. Therefore, a verification and validation procedure of the numerical model is necessary before the code can be applied to real-world problems [6].

A significant amount of research activity was conducted in the last years for Darrieus type small-scale wind turbines in order to improve their performance. Singh et. al. [3] adopted CFD approach to study the self-starting ability of VAWT. In their analysis the conventional straight blades were replaced with unsymmetrical ones and, in this way, the rotor solidity was increased.

Zamani et. al. [7] performed numerical analysis by using the software OpenFOAM. They studied how a J-shaped profile of the blades, designed from a DU 06-W-200 aerofoil, can improve the starting torque. These numerical investigations showed that the J-shaped profile removes the pressure side of aerofoil from the maximum thickness toward the trailing edge.

Naccache et al. [8] proposed an optimization of the Darrieus-type VAWT extending the high-power generation area of the blades, by using a dual axis wind turbine.

Some of the authors of the present paper, in previous research [9] analysed the performance of a real scale innovative configuration of Darrieus-type VAWT for small-scale power generation by means of 2D CFD investigations. The turbine was composed of three pairs of blades, each composed by a main and auxiliary aerofoil. The results of the simulations confirmed the capabilities of the investigate VAWT configuration to give valuable performance even for wind speeds below 4 $m \cdot s^{-1}$. The numerical results were validated in terms of bulk power and torque coefficients collected during wind tunnel experiments conducted at the University of Cassino and Southern Lazio, and it was observed that simulations and measurements were not compatible for very high Tip Speed Ration (TSR) [9], evidencing that a results validation in terms of local velocity field is actually required. In the present paper, measurements performed on a pair of the VAWT blades investigate in [9] by employing the Particle Image Velocimetry (PIV) technique are presented. Measurements are used to validate CFD results in terms of local air velocity distribution in correspondence of the aerofoils surface. According to the knowledge of the authors, a benchmark of VAWT composed by a pair of blades is proposed here for the first time.

In the last decades, PIV technique was adopted to produce quantitative flow velocity data for the validation of numerical simulations. In particular, Castelein [10] realized a benchmark of VAWT in dynamic stall. Edwards [11] realized PIV measurements and CFD simulation of the performance and flow physics of a small-scale VAWT. In his analysis, Edwards found significant CFD-PIV differences in predicting flow re-attachment. In particular, at a higher tip speed ratio, the flow separates slightly later than in the previous condition. The wake structure behind a vertical axis wind turbine (VAWT) was both measured in a wind tunnel using PIV and computed with large-eddy simulation (LES) by Posa [12]. The dependence of the wake structure on the Tip Speed Ratio (TSR) was investigated, showing higher asymmetry and larger vortices at the lower rotational speed, due to stronger dynamic stall phenomena. Lam [13] studied the wake characteristics of a vertical axis wind turbine by two- and three-dimensional computational fluid dynamics simulations. The wake velocity field and turbulence field from 1 to 10 turbine diameters (1D to 10D) downstream were examined. Both the transition Shear Stress Transport (SST) and the Detached Eddy Simulation (DES) models were used to close the unsteady Reynolds-averaged Navier-Stokes (URANS) equations. The CFD models were validated by PIV test results from the literature. The regions of the near and far wakes were defined based on the occurrence of the maximum velocity deficit. In the near wake (within 3D), the velocity suffered a drastic deficit of about 85%. In the far wake (beyond 3D), major velocity recovery occurred with the average stream-wise velocity reaching approximately 75% at 10D.

In this paper, the authors propose the validation of a numerical model, by PIV techniques, finalized to the determination of the velocity field around a pair of blades of an innovative Darrieus-type VAWT. In particular, the experimental and numerical velocity fields were obtained in correspondence of the main and auxiliary profile of the pair of blades, in static conditions (absence of blade rotation). Experiment were numerically reproduced by employing by employing CFD technique and modelling turbulence using the k-ω-SST and Spalart-Allmaras RANS (Reynolds Averaged Navier Stokes) turbulence models. The validated numerical model represents a valid and powerful tool allowing to analyze the effect of different geometric configurations and rotation angles on the turbine torque and power coefficients, with the aim to improve performance in urban applications.

2. METHODS

In this section the experimental analysis by PIV technique on a pair of not-rotating blades of an innovative Darrieus-type VAWT is illustrated. The experimental results were used in order to validate the numerical model. The validated numerical tool allows the velocity field determination around a pair of blades in different fluid-dynamic conditions.

2.1 Darrieus-type VAWT prototipe

The innovative VAWT configuration, investigated in the present paper by PIV technique, was selected by some of the authors in previous works finalized to the definition of the optimal geometrical parameters allowing the performance optimization in terms of torque and power coefficients [9], [14].

The analysed VAWT is composed of three pairs of blades placed at 120° each other. Each pair of blades presents the main and an auxiliary aerofoil, illustrated in Figure 1. The blades consists in a modified version of the DU 06-W-200 aerofoil available in the scientific literature [15].

The main aerofoil chord length, C_1, is equal to 68 mm and the ratio between main and auxiliary aerofoils chord lengths, C_2/C_1, is equal to 0.60, the angles of attack, α_1 and α_2, (the angles between the profile chord and the tangential velocity vector) are both fixed and equal to 12.5°; the distance between the two aerofoils, *y*, is equal to 18.40 mm, the longitudinal distance between the aerofoils, *x*, is equal to 25 mm., while the diameter and the height of the micro turbine model are equal to 120 mm and 140 mm respectively.

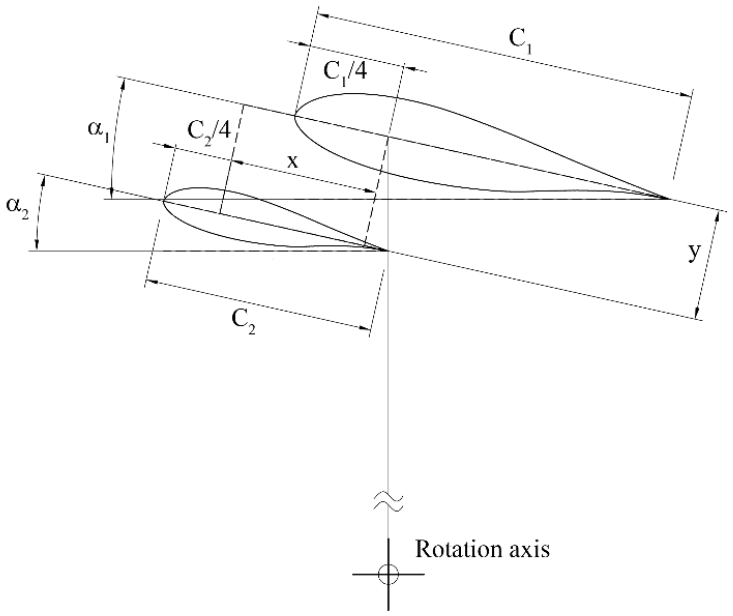

Figure 1. Geometrical configuration of the pair of blades investigated by PIV analysis.

PIV measurements were conducted on a 1:4 scale model realized with a 3D printer based on the "Fused Deoposition Modelling" (FDM).

2.2 Wind tunnel and PIV system setup

The wind tunnel of Laboratory of Industrial Measurements (LaMI) of the University of Cassino and Southern Lazio (Italy) was employed to perform experimental analysis on the pair of blades. The apparatus is located in a 150 m^3 room equipped with a mechanical ventilation system with an air exchange rate of 0.3 h^{-1}. In this way it is possible to get constant humidity and temperature values

equal to 20 ± 2 °C and 50 ± 5% RH, respectively. A schematic of the equipment is available in Figure 2. The wind tunnel of LaMI consists of the following components: an inlet nozzle (16:1 contraction ratio), flow conditioners (honeycombs), vortex generators, a flow establishment section, a test section, anti-swirl devices (honeycombs and grids) and a squirrel-cage centrifugal fan. The wind in the tunnel can reach a speed equal to 25 m/s by a DC motor equipped with a thyristor type control system. The wind tunnel manufacturer guarantees an expanded uncertainty, associated with air velocity measurements equal to 1.8% in the speed range 5÷20 m/s. Finally, the test chamber is of an Eiffel-type, with 1.1 m of height and 1.0 m of width. The wind tunnel of the LaMI is equipped with a Particle Image Velocimetry (PIV) measurement system, that allows 2D measurements of the air velocity field on a parallel plane with respect to the air flow direction, according to the laser light that illuminates the measurement area from the top of the test chamber, as reported in Figure 2.

The physical principle on which the PIV technique is based is the following: in a short period of time the laser light illuminates twice the flow seeded by micron-sized particles. The illuminated particles allow to obtain two distinct images and by a cross-correlation method the local velocity vectors are reconstructed [16]. The PIV analysis allows to get the instantaneous velocity field in 2D dimensions because the time interval is short compared to the flow time scales [17]. Details about such non-intrusive measurement technique are available in the scientific literature [18], [19] and are not reported here for brevity.

The Laser of the PIV system is a NANO L135-15 while the camera is a TSI PowerView Plus model 7002262 equipped with 50 mm - 1:1.8 Nikkor optics.

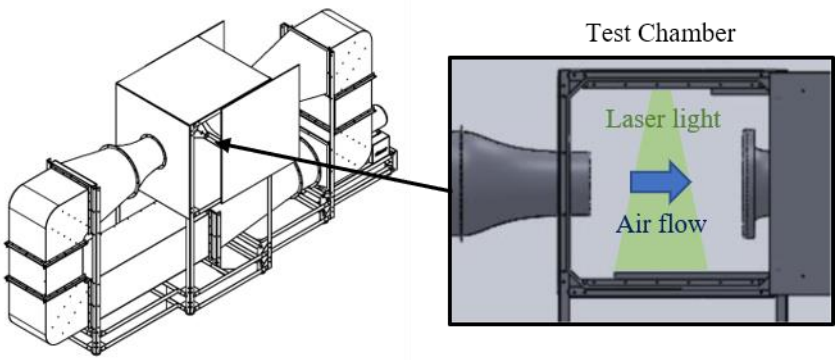

Figure 2. Wind tunnel available at the Laboratory of Industrial Measurements (LaMI).

2.3 Uncertainty analysis of the PIV measurements

The uncertainty analysis associated to the experimental data obtained by PIV system are based on the uncertainty propagation law [20]. A brief description of the procedure is reported below. The principle of the PIV measurement can be described by the following equation [21]:

$$w = \alpha \frac{\Delta x}{\Delta t} + \delta w \tag{1}$$

where w is the velocity (m/s), Δx represents the pixel displacement of particles between PIV image pairs, δw (m/s) takes into account particle velocity lag from fluid acceleration together with three-dimensional effects on prospective of the velocity field, and α (m/pixel) is the scaling magnification factor. The uncertainty associated to the PIV average velocity measurements can be evaluated by Equation 2:

$$u_w = \sqrt{u_A^2 + \left(\frac{\partial w}{\partial \alpha}\right)^2 u_\alpha^2 + \left[\frac{\partial w}{\partial(\Delta x)}\right]^2 u_{\Delta x}^2 + \left[\frac{\partial w}{\partial(\Delta x)}\right]^2 u_{\Delta t}^2 + u_{\delta w}^2} \tag{2}$$

where u_w is the measured velocity standard uncertainty, u_A is the type A uncertainty, that for the case under investigation was evaluated to be negligible with respect to other uncertainty contributions, while u_α, $u_{\Delta x}$, $u_{\Delta t}$, $u_{\delta w}$ represent the standard uncertainties of different influence parameters. In particular, the magnification factor is defined as:

$$\alpha = \frac{l_r \cos(\vartheta)}{L_r} \simeq \frac{l_r(1 - \frac{\vartheta^2}{2})}{L_R} \tag{3}$$

where l_r is the distance of the reference point expressed in mm, L_r is the distance of reference image expressed in pixel, ϑ is the prospective angle. The standard uncertainty of the magnification factor was evaluated by means of the following propagation law:

$$u_a = \sqrt{\left(\frac{\partial \alpha}{\partial L_R}\right)^2 \left({u_{L_R}}^2 + {u_{l_t}}^2\right) + \left(\frac{\partial \alpha}{\partial l_r}\right)^2 {u_{l_r}}^2 + \left(\frac{\partial \alpha}{\partial \vartheta}\right)^2 {u_\vartheta}^2 + \left(\frac{\partial \alpha}{\partial \theta_0}\right)^2 {u_{\theta_0}}^2} \tag{4}$$

where u_{lt} represents the standard uncertainty of the distance from target l_t, u_{lr} and u_{Lr} were evaluated as the ratio between the resolution (in meters and pixels, respectively) and $\sqrt{3}$, resulting in: $u_{l_r} = \frac{0.001}{\sqrt{3}}\ m$ and $u_{L_r} = \frac{1}{\sqrt{3}}\ pixel$. Similarly, the value of $u_{\Delta x}$ was evaluated as the ratio between the maximum error in the evaluation of x-displacement and $\sqrt{3}$, resulting in:

$$u_{\Delta x} = \frac{\left(d_p\ 1.2 \times 10^{-6}\right)}{\sqrt{3}}\ \ m \tag{5}$$

where the maximum error is evaluated as the mean diameter of the particles d_p $(1.2 \times 10^{-6}\ m)$. Finally, $u_{\Delta x}$ was considered to be negligible with respect to the other uncertainty contributions. The 3D effects on the prospective of velocity were evaluated as indicated in the following:

$$u_{\delta w} = 0.03\ U_{REF} \cdot \tan(\vartheta) \tag{6}$$

where U_{REF} is the uniform flow speed and ϑ is the prospective angle.

2.4 Mathematical and numerical models

The numerical analysis was performed using the open source software OpenFOAM. The fluid flow impacting the pair of blades was investigated by solving the mass and momentum conservation equations, and modelling the turbulence phenomena adopting an Unsteady Reynolds Averaged Navier-Stokes (URANS) model. Details about the employed partial differential equations are available in the scientific literature [9], [22] and are not reported here for brevity. On the basis of results presented in [9], two different turbulence models were employed for numerical investigations: the SST k-ω and the Spalart-Allmaras turbulence models. Simulations were conducted in a bi-dimensional domain and in transient state, using a time step value equal to $1 \cdot 10^{-5} s$, and employing a second order discretization scheme for the upwind scheme. In Figure 3 the computational domain and the boundary conditions employed are illustrated. At the inlet section, a constant and uniform x-component of the velocity equal to 10 m/s with a turbulence intensity equal to 0.5% was imposed, reproducing the measured average velocity and turbulence intensity from PIV measurements. Besides, the distance between inlet section and auxiliary airfoil was set to 300 mm to reproduce model placement in the test chamber of the wind tunnel. Symmetry condition was applied at the top and bottom sides of the domain, zero pressure at the outlet section and no slip condition on solid blade surfaces. The whole computational domain is 340 mm height (equal to 5 times the chord lengths of the main blade) and 680 mm width (equal to 10 times the chord lengths of the main blade).

The reference system is placed at the leading edge of the auxiliary blade, 300 mm from the inlet section. Simulation were performed employing the unstructured computational grid available in Figure 4, that is composed by 1709097 cells chosen on the basis of a proper mesh sensitivity analysis. In order to reproduce the velocity filed in the wake and in correspondence of airfoils sold surfaces, the grid was refined in the wake region and near the walls, where a “viscous layer” was applied with a number of layers equal to 10, a minimum mesh size of $9x10^{-5}$ m and a growth rate of 1.1. The maximum computational grid size in the free stream is equal to 1.2 mm.

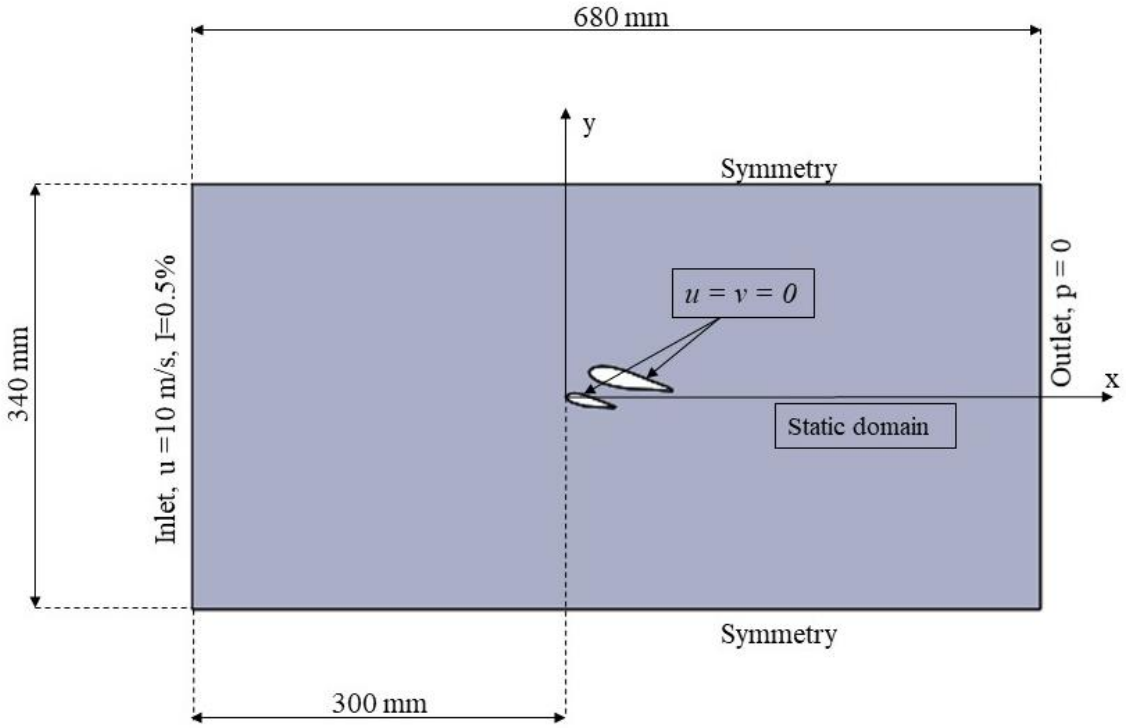

Figure 3. Computational domain and boundary conditions employed for the numerical simulations.

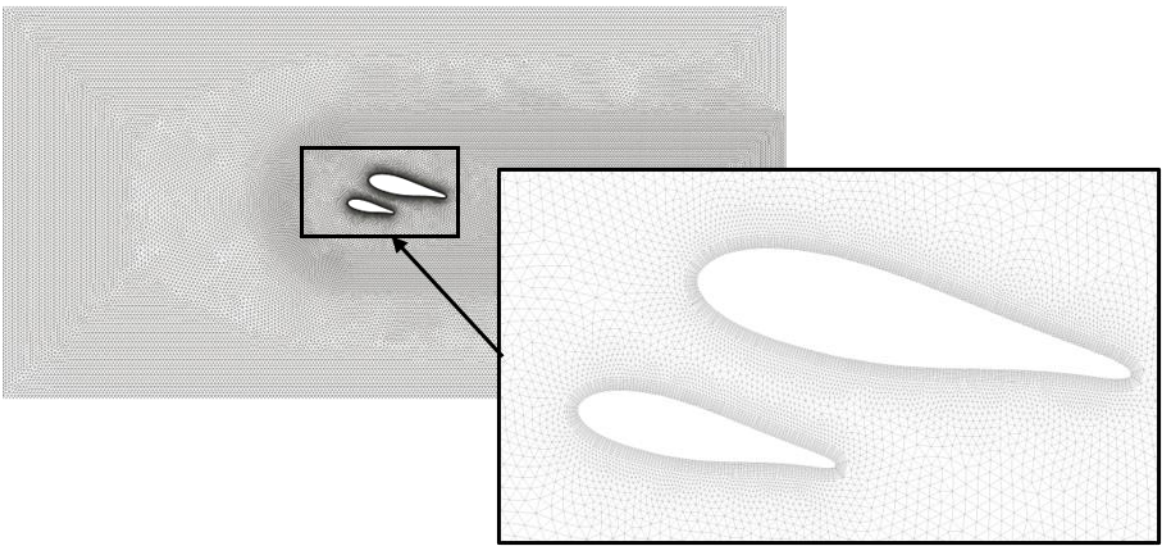

Figure 4. Computational grid composed by 1709097 cells.

3. RESULTS

3.1 Experimental results

Since laser light that illuminates the prototype for PIV measurements comes from the top of the wind tunnel test chamber and no measurement is possible in shadow areas, two models have been realized: the Model 1 has been realized adopting the geometrical configuration illustrated in Figure 1, while the Model 2 has been obtained by mirroring the first one with respect to horizontal plane. This allowed to perform two different PIV tests: Test 1, conducted on Model 1; Test 2, performed on Model 2. Test

1 and Test 2 were clearly performed at the same air velocity and at the same position in the test chamber of the wind tunnel. Therefore, in Test 1 allowed to measure the velocity field only on the top of the prototype, while Test 2 allowed measurements on the bottom side. In Table 1, the configuration parameters selected for the two tests are listed.

Table 1. PIV configuration parameters

Step	**Description**	**PIV Test 1 illumination from the top**	**PIV Test 2 illumination from the bottom**
Adjustment	Object distance from millimetres to pixels	130x 1868 px	120x 1628 px
Lens distance	The physical distance between the camera lens and the section illuminated by the laser	51 cm	51 cm
Engine power	Percentage of the wind tunnel engine – wind velocity	28% - 10 m/s	28% - 10 m/s
Lens opening	Size of the lens aperture	4	4
Laser A energy	Energy emitted by the laser during the frame A acquisition	800mJ	700 mJ
Laser B energy	Energy emitted by the laser during the frame B acquisition	820mJ	780 mJ
Frequency	Acquisition frequency of the photographs	7.25 Hz	7.25 Hz
Time	Time interval between the frame A and frame B capture	0.00000021 s	0.00000021 s
Interrogation cell	Interrogation cell dimensions	from 16x16 to 32x32	from 16x16 to 32x32

In Figure 5, the blades image taken in the wind tunnel are reported. In particular, fog particles and instantaneous velocity vectors reconstruction during Test 1 (measurement from the top) are illustrated in Figure 5(a) and Figure 5(b) respectively, while fog particles and instantaneous velocity vectors reconstruction during Test 2 (measurement from the bottom) are illustrated in Figure 5(c) and Figure 5(d) respectively.

The averaged velocity contours, obtained by averaging 1500 PIV instantaneous measurements are reported in Figure 6(a) and Figure 6(b) for Test 1 and Test 2, respectively. From the figure it is possible to observe a distortion of the flow lines and a vortex shedding phenomenon at the leading edge of the auxiliary blade.

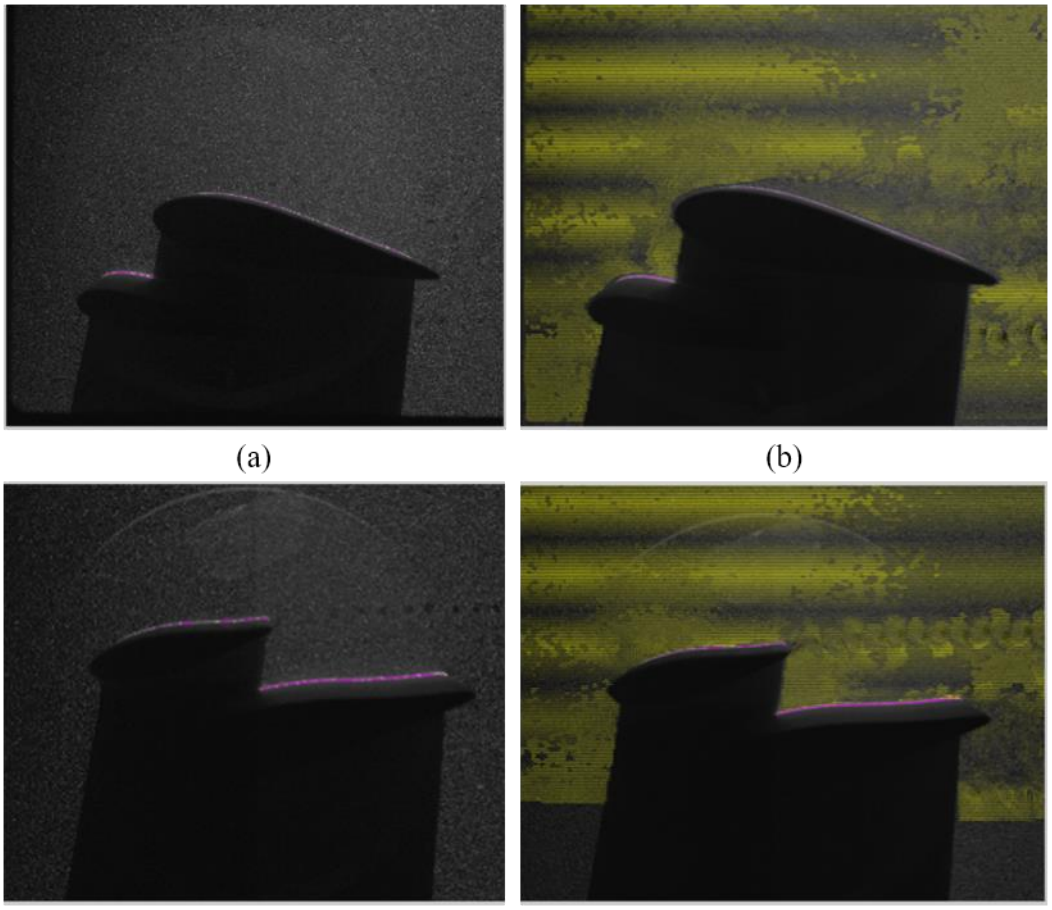

Figure 5. Image of the blades taken in the wind tunnel. Fog particles (a) and velocity vectors reconstruction (b) during Test 1; fog particles (c) and velocity vectors reconstruction (d) during Test 2.

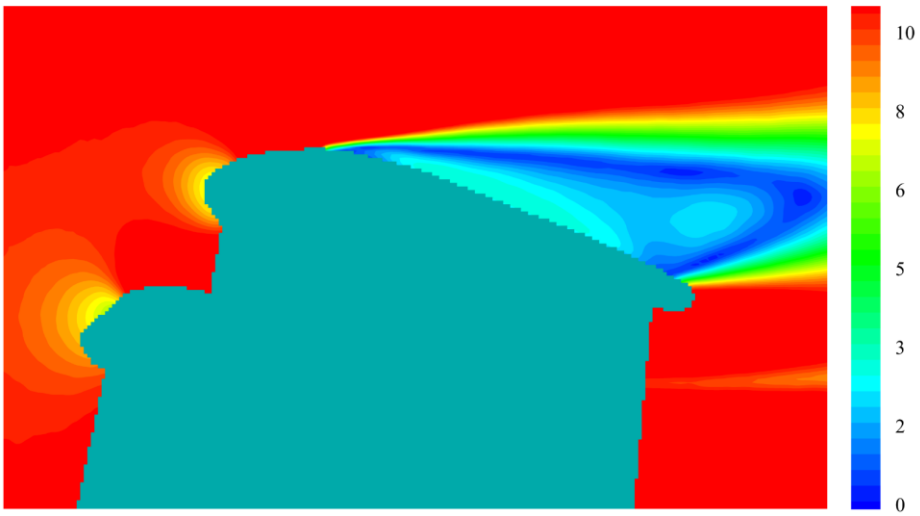

(a)

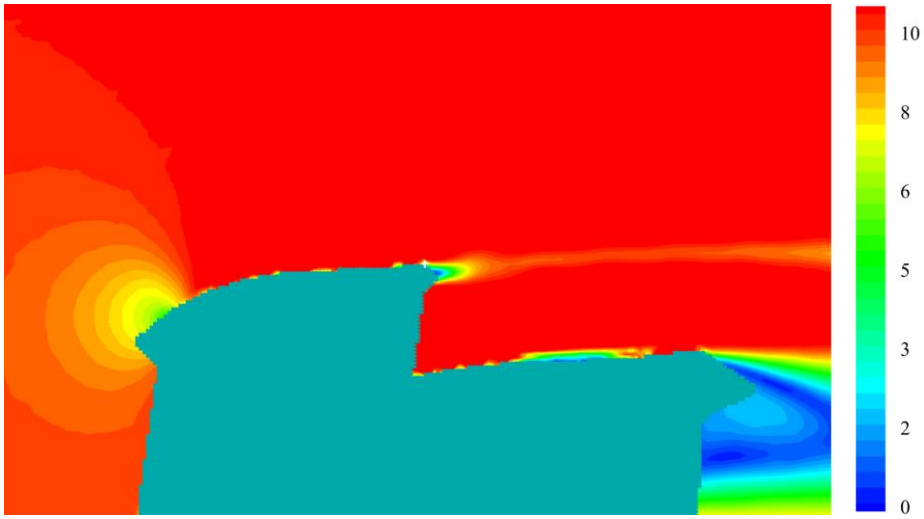

(b)

Figure 6. Averaged velocity (m/s) contours for Test 1 (a) and for Test 2 (b).

3.2 Statistical convergence

In order to evaluate the required number of acquisitions for the statistical convergence, a convergence analysis was performed in correspondence of sections P1, P2 and P3 for both Test 1 and Test 2 (see Table 7). In particular, 250 instantaneous velocity acquisitions have been added for the calculation of the averaged fields at each step of the sensitivity analysis, until the percentage deviation was observed to be below 1% between two successive steps. In Figure 7 the results of the statistic convergence are illustrated in terms of u-velocity and v-velocity–average errors as a function of the acquisitions number. From the analysis of obtained results it derives that an acquisition number equal to 1000 was sufficient to get an error below 1% (Figure 7a, Figure 7c and Figure 7e) ensuring the statistic convergence for Test 1, while for Test 2 an acquisition number of 1500 images was necessary in order to limit the error (Figure 7b, Figure 7d, Figure 7f) not larger than 1%.

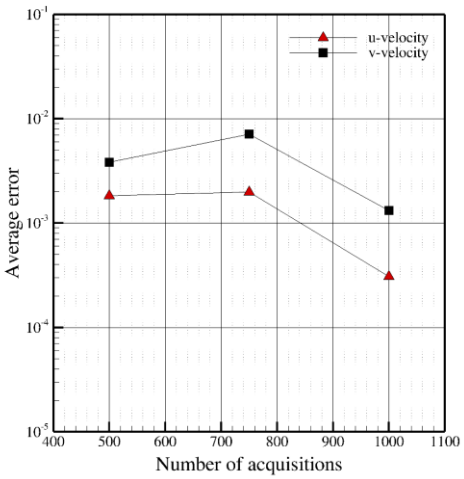

(a)

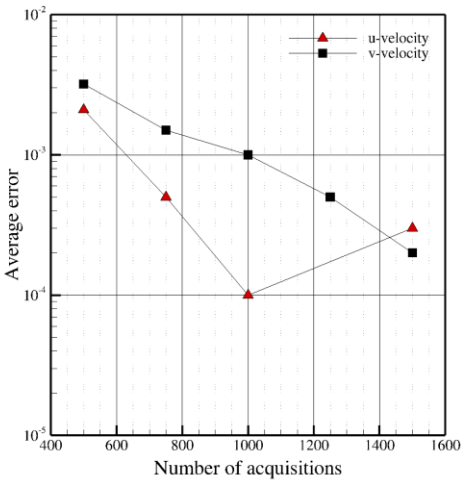

(b)

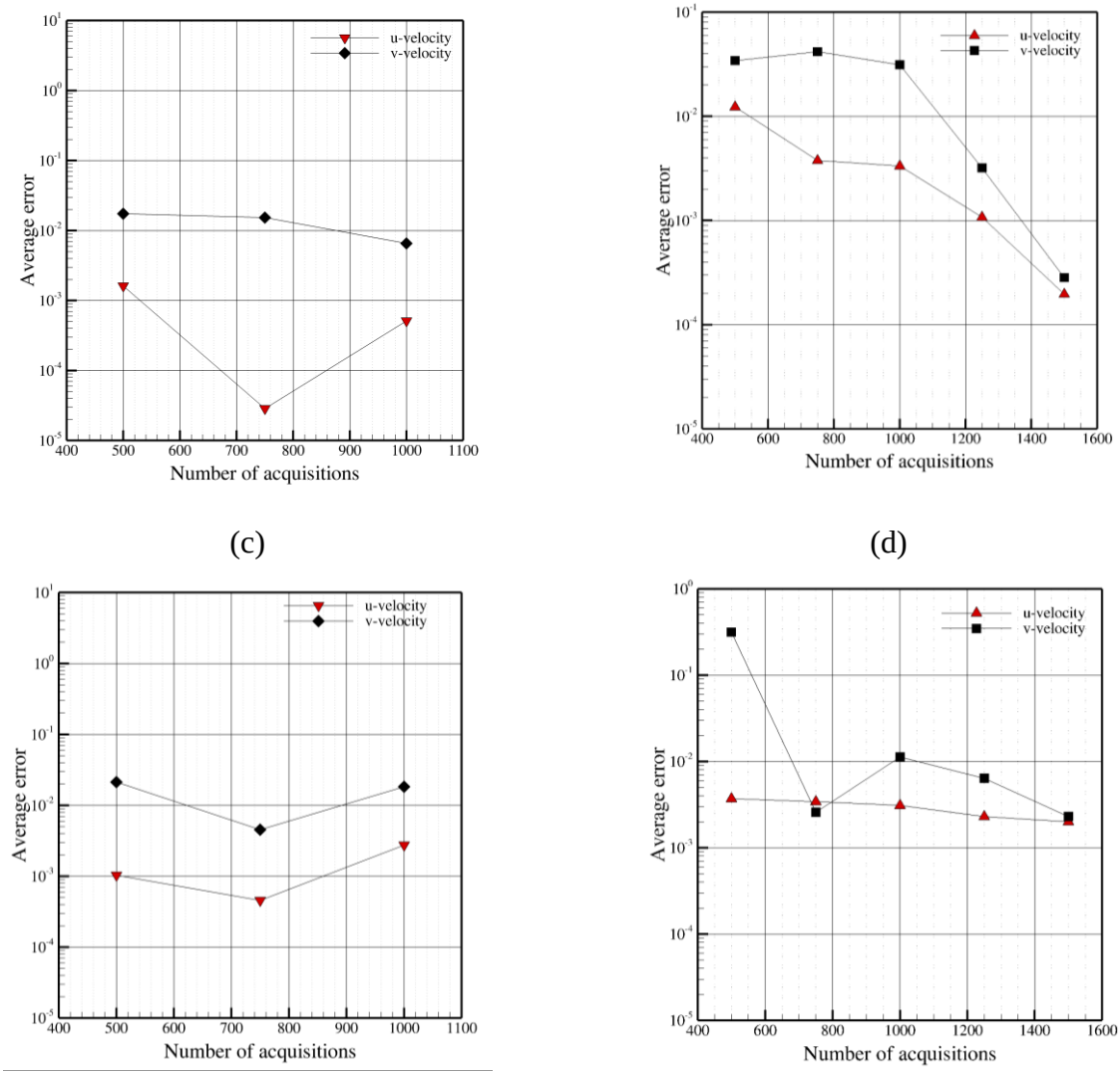

Figure 7. Results of the statistic convergence. Average error as a function of the number of acquisitions obtained in correspondence of the profile P1 for Test 1 (a) and Test 2 (b), in correspondence of the profile P2 for Test 1 (c) and Test 2 (d), in correspondence of the profile P3 for Test 1 (e) and Test 2 (f).

3.3 Uncertainty analysis results

In order to perform the uncertainty analysis, it is necessary to evaluate the relative standard uncertainty of all the contributions. The input parameters necessary to perform PIV measurements are listed in Table 2.

Table 2. Input parameters used for PIV measurements

Parameter	**Test 1**	**Test 2**
Measurement area (square) [m]	0.12	0.13
Uniform flow speed [m/s]	9.72	9.72
Magnification factor, alfa [m/px]	7.11E-05	7.11E-05
Distance of reference points, lr [m]	0.12	0.13

Distance of reference image, Lr [px]	1688	1828
Time interval [s]	0.000021	0.000021
Distance from target, lt [m]	0.585	0.585
Camera resolution [px]	2048	2048
Sampling frequence [Hz]	7.25	7.25
Particles average diameter [m]	1.20E-06	1.20E-06
Correlazion area size [px]	16	16

The results of the standard uncertainty contributions for Test 1 are listed in Table 3.

Table 3. Standard uncertainty of the calibration factors

	Uncertainty source	Parameter	Sensitivity coefficient	Standard uncertainty
Calibration board	Distance of reference image	L_r	$\frac{\partial \alpha}{\partial L_r} = -\frac{l_r}{{L_r}^2} = -4.21x10^{-8}\frac{m}{px^2}$	$u_{L_r} = \frac{1}{\sqrt{3}} = 5.77x10^{-1}\,px$
	Distance of reference points	l_r	$\frac{\partial \alpha}{\partial l_r} = \frac{1}{{l_r}^2} = 5.92x10^{-4}\frac{1}{px}$	$u_{l_r} = \frac{1.00x10^{-3}}{\sqrt{3}} = 5.77x10^{-4}\,px$
Optical system	Image distortion	0.5% L_r	$\frac{\partial \alpha}{\partial L_r} = -\frac{l_r}{{L_r}^2} = -4.21x10^{-8}\frac{m}{px^2}$	$u_{Dis} = \frac{0.005xL_r}{\sqrt{3}} = 4.87px$
Experimental condition	Reference board position	l_t	$\frac{\partial \alpha}{\partial l_t} = \frac{l_r}{l_t L_r} = 1.22x10^{-4}\frac{1}{px}$	$u_{l_t} = \frac{5.00x10^{-3}}{\sqrt{3}} = 5.77x10^{-3}\,m$
	Parallel reference board	ϑ	$\frac{\partial \alpha}{\partial \vartheta} = -\frac{l_r \vartheta}{L_r} = -2.48x10^{-6}\frac{m}{px}$	$u_\vartheta = \frac{2\cdot\pi}{180\sqrt{3}} = 0.020\,rad$
Image detection	Normal vie angle	θ_0	$\frac{\partial \alpha}{\partial \theta_0} = -\frac{l_r \theta_0}{L_r} = -2.48x10^{-6}\frac{m}{px}$	$u_{u_{\vartheta_0}} = \frac{2\cdot\pi}{180\sqrt{3}} = 0.020\,rad$

The standard uncertainty of the scaling magnification factor (u_a) evaluated by means of Equation (7) is equal to $8.11\,x10^{-7}$m/px. Then, the evaluation of the remaining sensitivity coefficients with the relative standard uncertainties was performed, as shown in Table 4.

Table 4. Contributions for the composed velocity uncertainty calculation for Test 1

	Uncertainty source	Standard uncertainty	Sensitivity coefficient	Standard uncertainty
	Type A uncertainty	u_A	-	0.1 m/s
Velocity sensitivity coefficients	Scaling magnification factor	u_a	$\frac{\partial u}{\partial \alpha} = 1.37x10^5\frac{\text{px}}{\text{s}}$	$8.11\,x10^{-7}$ m/px
	Displacement of particle image	$u_{\Delta x}$	$\frac{\partial u}{\partial(\Delta x)} = \frac{\alpha}{\Delta t} = 3.39\frac{m\,px}{s}$	$9.75\,x10^{-3}$ px
	Time interval	$u_{\Delta t}$	$\frac{\partial u}{\partial(\Delta t)} = \frac{\partial u}{\partial(\delta u)} = 1\,s$	0.000021 s

Particle Trajectory	3D effects on prospective of velocity	$u_{\delta w}$	-	0.074 m/s

Finally, as a result of the uncertainty analysis for Test 1, it was found that the composed velocity uncertainty, calculated by Equation (8), assuming a coverage factor k=2 (confidence level 95%), was equal to 0.17 m/s. Similarly, the results of the standard uncertainty contributions for Test 2 are listed in Table 5.

Table 5. Standard uncertainty of the calibration factors

	Uncertainty source	Parameter	Sensitivity coefficient	Standard uncertainty
Calibration board	Distance of reference image	L_r	$\frac{\partial \alpha}{\partial L_r} = -\frac{l_r}{{L_r}^2} = -3.89x10^{-8}\frac{m}{px^2}$	$u_{L_r} = \frac{1}{\sqrt{3}} = 5.77x10^{-1}\,px$
	Distance of reference points	l_r	$\frac{\partial \alpha}{\partial l_r} = \frac{1}{{l_r}^2} = 5.47x10^{-4}\frac{1}{px}$	$u_{l_r} = \frac{1.00x10^{-3}}{\sqrt{3}} = 5.77x10^{-4}\,px$
Optical system	Image distortion	0.5% L_r	$\frac{\partial \alpha}{\partial L_r} = -\frac{l_r}{{L_r}^2} = -3.89x10^{-8}\frac{m}{px^2}$	$u_{Dis} = \frac{0.005xL_r}{\sqrt{3}} = 5.28px$
Experimental condition	Reference board position	l_t	$\frac{\partial \alpha}{\partial l_t} = \frac{l_r}{l_t L_r} = 1.22x10^{-4}\frac{1}{px}$	$u_{l_t} = \frac{5.00x10^{-3}}{\sqrt{3}} = 5.77x10^{-3}\,m$
	Parallel reference board	ϑ	$\frac{\partial \alpha}{\partial \vartheta} = -\frac{l_r \vartheta}{L_r} = -2.48x10^{-6}\frac{m}{px}$	$u_{\vartheta} = \frac{2\cdot\pi}{180\sqrt{3}} = 0.020\,rad$
Image detection	Normal vie angle	θ_0	$\frac{\partial \alpha}{\partial \theta_0} = -\frac{l_r \theta_0}{L_r} = -2.48x10^{-6}\frac{m}{px}$	$u_{u_{\vartheta_0}} = \frac{2\cdot\pi}{180\sqrt{3}} = 0.020\,rad$

The standard uncertainty of the scaling magnification factor, evaluated by means of Equation (9) for Test 2 is equal to $8.00\,x10^{-7}$m/px. Then, the evaluation of the remaining sensitivity coefficients with the relative standard uncertainties was performed, as shown in Table 6. Finally, as a result of the uncertainty analysis for Test 2, it was found that the composed velocity uncertainty, calculated by Equation (10) assuming a coverage factor k=2 (confidence level 95%), was equal to 0.17 m/s.

Table 6. Contributions for the composed velocity uncertainty calculation for Test 2

	Uncertainty source	Standard uncertainty	Sensitivity coefficient	Standard uncertainty
	Type A uncertainty	u_A	-	0.1 m/s
Velocity sensitivity coefficients	Scaling magnification factor	u_a	$\frac{\partial u}{\partial \alpha} = 1.37x10^5\frac{\text{px}}{\text{s}}$	$8.00\,x10^{-7}$ m/px
	Displacement of particle image	$u_{\Delta x}$	$\frac{\partial u}{\partial(\Delta x)} = \frac{\alpha}{\Delta t} = 3.39\frac{m\,px}{s}$	$9.74\,x10^{-3}$ px
	Time interval	$u_{\Delta t}$	$\frac{\partial u}{\partial(\Delta t)} = \frac{\partial u}{\partial(\delta u)} = 1\,s$	0.000021 s

Particle Trajectory	3D effects on prospective of velocity	$u_{\delta w}$	-		0.074 m/s

3.4 Numerical model validation and results

In order to validate the CFD model, in this section the numerical and PIV data are compared and analyzed. In particular, the comparisons are shown in terms of horizontal (u) and vertical (v) components of the velocity in the four different vertical sections across the wind turbine airfoils indicated in Table 7 and schematically reported in Figure 8.

Table 7. Geometric coordinates of the velocity profiles extracted along the blades.

Profile	x-coordinate [mm]	y-coordinate [mm]
Reference	0	from 40 to -40
P1	10	from 40 to -40
P2	30	from 40 to -40
P3	50	from 40 to -40
P4	70	from 40 to -40

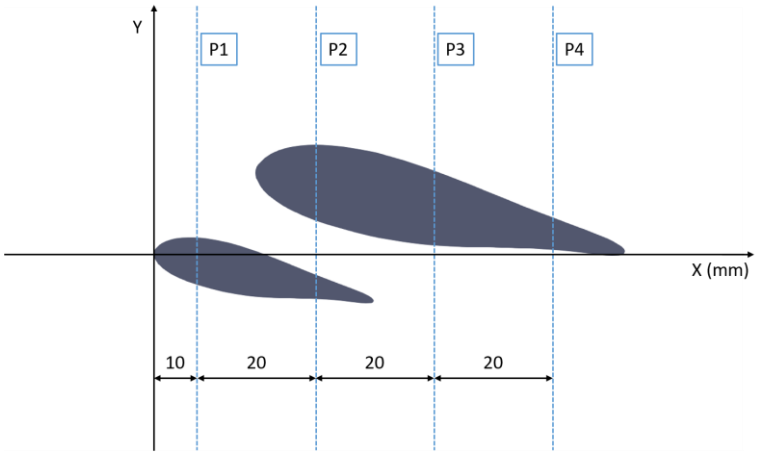

Figure 8. Different sections across the wind turbine blades in which the horizontal and vertical components of the velocity are compared with the PIV measurements.

The figures 10 and 11 show the PIV data measured in the wind tunnel as well as the numerical results obtained with the SST k-ω and the Spalart-Allmaras (S-A) turbulence models.

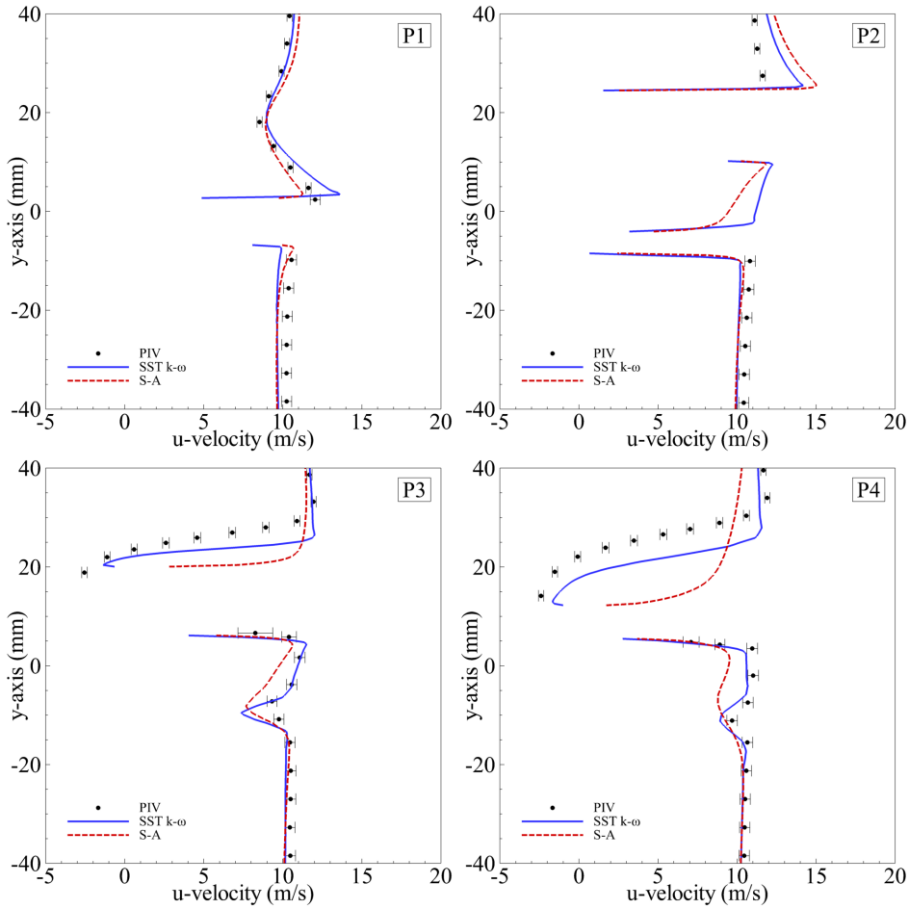

Figure 9. Comparison between CFD and PIV results in terms of horizontal component of the velocity (u) in different vertical sections across the wind turbine blades.

On the basis of the velocity data reported in Figure 9 and Figure 10, it is possible to observe that the SST k-ω turbulence model shows an overall better ability to reproduce the flow pattern around the airfoils if compared to the PIV measured data. In particular, looking at the u-velocity profiles on the upper surface of the main airfoil, it is clear that the S-A turbulence model is not able to reproduce the flow separation observed in the PIV measurements at the considered angle of attack (Figure 6). In fact, while both the turbulence models perform in a satisfying way as long as the fluid remains attached to the surface (upper sides of P1 and P2 in Figure 9), when the flow starts to separate, the S-A model fails to correctly visualize such separation, while the SST k-ω model is able to reproduce the recirculation zone due to such flow separation (upper sides of P3 and P4 in Figure 9).

Looking at the v-velocity profiles of Figure 10, the same behaviour can be observed as for the u-velocity, with an overall better performance of the SST k-ω model, which is able at least to reproduce the shape of the experimental profiles where the S-A model largely fails, especially in the high separation zone of the main airfoil upper surface (upper sides of the v-velocity profiles P3 and P4, Figure 10).

Overall, it can be seen from Figure 9 and Figure 10 that the flow pattern on the lower surface of the blades results correctly reproduced by both the considered turbulence models since in such a zone

there is no significant flow separation at the considered angle of attack, as observed in Figure 6. However, some discrepancies between the models are observable in the zone immediately after the trailing edge of the auxiliary blades, where the flow tends to decelerate in the x direction. In this zone, in fact, both the models tend to follow the shape of the experimental profile (Figure 9), but the SST k-ω model once again performs better with respect to the S-A.

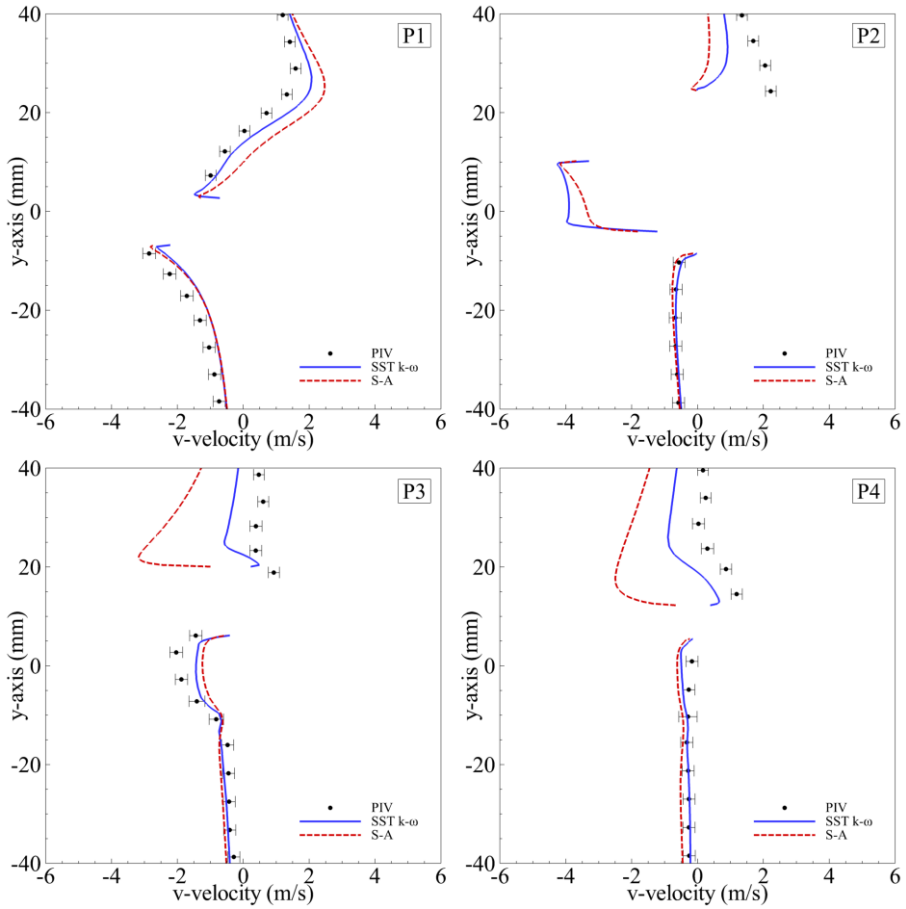

Figure 10. Comparison between CFD and PIV results in terms of vertical (along y) component of the velocity (u) in different vertical sections across the wind turbine blades.

4. CONCLUSIONS

In this paper, the authors propose the validation of a numerical model, by PIV techniques, finalized to the determination of the velocity field around a pair of blades of an innovative Darrieus-style Vertical Axis Wind Turbine (VAWT) in static conditions (absence of blade rotation).

The turbine configuration, already proposed in our previous works and analysed for a scaled model in a wind tunnel, is composed of three couple of aerofoils (main and auxiliary) and has shown good capabilities to operate even for wind speeds below 4 $m \cdot s^{-1}$ (domestic applications). A preliminary numerical model, able to predict the wind turbine performances, was only validated by using bulk data as the power and torque coefficients, collected during wind tunnel experiments, highlighting that

the agreement between experimental and numerical data was not obtained in all the analysed operating conditions.

In the present work, in order to optimize the performance of the numerical model and verify the suitability of the numerical model, 2D Unsteady Reynolds Averaged Navier-Stokes (URANS) simulations are made out using the open-source OpenFOAM CFD software. Results from SST k-ω and the Spalart-Allmaras turbulence models, in terms of horizontal and vertical components of the velocity over the aerofoils surface, are compared with experimental data from wind tunnel investigation made out with Particle Image Velocimetry (PIV) technique. In order to experimentally analyse the wake flow characteristics with PIV method, a scale model of a pair of blades is realised by means of 3D printer. The printed model is adequately studied in a closed-circuit wind tunnel facility available in the Laboratory of Industrial Measurement (LaMI) of the University of Cassino and Lazio Meridionale.

From the numerical analysis, it is possible to state that the SST k-ω turbulence model shows an overall better ability to reproduce the flow pattern around the airfoils if compared to the PIV measured data. The flow pattern on the lower surface of the blades results correctly reproduced by both the considered turbulence models since in such a zone there is no significant flow separation at the considered angle of attack. Some discrepancies between the models are observable in the zone immediately after the trailing edge of the auxiliary blade, where both the models tend to follow the shape of the experimental profile, but the SST k-ω model performs better with respect to the S-A.

According to the knowledge of the authors, a benchmark of VAWT composed by a pair of blades is proposed here for the first time. The validated numerical tool represents a valid and powerful tool allowing to analyze the effect of different geometric configurations and rotation angles of the blades on the turbine performances.

5. REFERENCES

[1] Y. Bazilevs, A. Korobenko, X. Deng, J. Yan, M. Kinzel, e J. O. Dabiri, «Fluid-structure interaction modeling of vertical-axis wind turbines», *J Appl Mech Trans ASME*, vol. 81, n. 8, 2014, doi: 10.1115/1.4027466.

[2] J. V. Akwa, H. A. Vielmo, e A. P. Petry, «A review on the performance of Savonius wind turbines», *Renewable Sustainable Energy Rev*, vol. 16, n. 5, pagg. 3054–3064, 2012, doi: 10.1016/j.rser.2012.02.056.

[3] M. A. Singh, A. Biswas, e R. D. Misra, «Investigation of self-starting and high rotor solidity on the performance of a three S1210 blade H-type Darrieus rotor», *Renew. Energy*, vol. 76, pagg. 381–387, 2015, doi: 10.1016/j.renene.2014.11.027.

[4] A. R. Sengupta, A. Biswas, e R. Gupta, «Studies of some high solidity symmetrical and unsymmetrical blade H-Darrieus rotors with respect to starting characteristics, dynamic performances and flow physics in low wind streams», *Renew. Energy*, vol. 93, pagg. 536–547, 2016, doi: 10.1016/j.renene.2016.03.029.

[5] A. G. Malan, R. W. Lewis, e P. Nithiarasu, «An improved unsteady, unstructured, artificial compressibility, finite volume scheme for viscous incompressible flows: Part I. Theory and implementation», *Int. J. Numer. Methods Eng.*, vol. 54, n. 5, pagg. 695–714, 2002, doi: 10.1002/nme.447.
[6] C. J. Roy, «Review of code and solution verification procedures for computational simulation», *J. Comput. Phys.*, vol. 205, n. 1, pagg. 131–156, 2005, doi: 10.1016/j.jcp.2004.10.036.
[7] M. Zamani, M. J. Maghrebi, e S. R. Varedi, «Starting torque improvement using J-shaped straight-bladed Darrieus vertical axis wind turbine by means of numerical simulation», *Renew. Energy*, vol. 95, pagg. 109–126, 2016, doi: 10.1016/j.renene.2016.03.069.
[8] G. Naccache e M. Paraschivoiu, «Development of the Dual Vertical Axis Wind Turbine Using Computational Fluid Dynamics», *J Fluids Eng Trans ASME*, vol. 139, n. 12, 2017, doi: 10.1115/1.4037490.
[9] F. Arpino, M. Scungio, e G. Cortellessa, «Numerical performance assessment of an innovative Darrieus-style vertical axis wind turbine with auxiliary straight blades», *Energy Convers. Manage.*, vol. 171, pagg. 769–777, 2018, doi: 10.1016/j.enconman.2018.06.028.
[10] D. Castelein, D. Ragni, G. Tescione, C. J. Simão Ferreira, e M. Gaunaa, «Creating a benchmark of vertical axis wind turbines in dynamic stall for validating numerical models», presentato al 33rd Wind Energy Symposium, 2015.
[11] J. M. Edwards, L. A. Danao, e R. J. Howell, «PIV measurements and CFD simulation of the performance and flow physics and of a small-scale vertical axis wind turbine», *Wind Energy*, vol. 18, n. 2, pagg. 201–217, 2015, doi: 10.1002/we.1690.
[12] A. Posa, C. M. Parker, M. C. Leftwich, e E. Balaras, «Wake structure of a single vertical axis wind turbine», *International Journal of Heat and Fluid Flow*, vol. 61, pagg. 75–84, 2016, doi: 10.1016/j.ijheatfluidflow.2016.02.002.
[13] H. F. Lam e H. Y. Peng, «Study of wake characteristics of a vertical axis wind turbine by two- and three-dimensional computational fluid dynamics simulations», *Renewable Energy*, vol. 90, pagg. 386–398, 2016, doi: 10.1016/j.renene.2016.01.011.
[14] M. Scungio, F. Arpino, V. Focanti, M. Profili, e M. Rotondi, «Wind tunnel testing of scaled models of a newly developed Darrieus-style vertical axis wind turbine with auxiliary straight blades», *Energy Convers. Manage.*, vol. 130, pagg. 60–70, 2016, doi: 10.1016/j.enconman.2016.10.033.
[15] M. Claessens, «The Design and Testing of Airfoils in Small Vertical Axis Wind Turbines», gen. 2006.
[16] R. D. Keane e R. J. Adrian, «Theory of cross-correlation analysis of PIV images», *Appl Sci Res (The Hague)*, vol. 49, n. 3, pagg. 191–215, 1992, doi: 10.1007/BF00384623.
[17] M. Stanislas e J. C. Monnier, «Practical aspects of image recording in particle image velocimetry», *Meas. Sci. Technol.*, vol. 8, n. 12, pagg. 1417–1426, 1997, doi: 10.1088/0957-0233/8/12/006.
[18] E. Lazar, B. DeBlauw, N. Glumac, C. Dutton, e G. Elliott, «A practical approach to PIV uncertainty analysis», in *AIAA Aerodyn. Meas. Ground Test. Conf.*, Chicago, IL, 2010.
[19] M. Raffel, C. E. Willert, S. Wereley, e J. Kompenhans, *Particle Image Velocimetry. A Practical Guide*. Springer-Verlag Berlin Heidelberg, 2007.
[20] «ISO/IEC Guide 98-3:2008. Uncertainty of measurement - Part 3: Guide to the expression of uncertainty in measurement (GUM: 1995)», 2008.
[21] S. Niscio, «Uncertainty analysis: Particle imaging velocimetry (PIV).», presentato al Uncertainty analysis: Particle imaging velocimetry (PIV)., 2008, vol. Section 75-01-03-03.
[22] F. Arpino, N. Massarotti, A. Mauro, e P. Nithiarasu, «Artificial compressibility-based CBS scheme for the solution of the generalized porous medium model», *Numer Heat Transfer Part B Fundam*, vol. 55, n. 3, pagg. 196–218, 2009, doi: 10.1080/10407790802628838.